Title

Shadow is related to roughness but MODIS BRDF should not be used to estimate lateral cover

Author

Okin, Gregory S

Publication Date

2023-07-01

DOI

10.1016/j.rse.2023.113581

Remote Sensing of Environment 292 (2023) 113581

Contents lists available at ScienceDirect

Remote Sensing of Environment

journal homepage: www.elsevier.com/locate/rse

Shadow is related to roughness but MODIS BRDF should not be used to estimate lateral cover

Gregory S. Okin

Department of Geography, University of California, Los Angeles, CA 90095, USA

ARTICLE INFO

Edited by Jing M. Chen

Keywords:
Dust
Shade
Surface roughness
MODIS
Albedo
Geometric-optical modeling

ABSTRACT

A simple geometric-optical model is used to show that shadow in optical remote sensing imagery contains information about surface roughness. The use of MODIS albedo products for the purpose of estimating surface roughness so that these products may aid in dust emission modeling has been proposed in previous studies (Chappell et al. 2010; Chappell and Webb 2016; Chappell et al. 2018). This approach is evaluated through geometric-optical modeling and by analysis of existing MODIS data. Little support is found for the utility of this approach for dust emission modeling. However, because there is clearly information about surface roughness in optical satellite imagery, some suggestions for the proper use of optical data to estimate surface roughness are made.

Chappell, A., Van Pelt, S., Zobeck, T., & Dong, Z. (2010). Estimating aerodynamic resistance of rough surfaces using angular reflectance. *Remote Sensing of Environment, 114*, 1462–1470.

Chappell, A., & Webb, N.P. (2016). Using albedo to reform wind erosion modeling, mapping and monitoring. *Aeolian Research, 23*, 63–78.

Chappell, A., Webb, N.P., Guerschman, J.P., Thomas, D.T., Mata, G., Handcock, R.N., Leys, J.F., & Butler, H.J. (2018). Improving ground cover monitoring for wind erosion assessment using MODIS BRDF parameters. *Remote Sensing of Environment, 204*, 756–768.

1. Introduction

Atmospheric mineral dust (also called mineral aerosols) is an important component of the Earth's system, with direct (e.g., Sokolik and Toon, 1996) and indirect (e.g., Lohmann and Feichter, 2005) effects on atmospheric radiative transfer as well as influences on precipitation (e.g., Yu et al., 2015), biogeochemistry (e.g., Jickells et al., 2005; Mahowald et al., 2005; Okin et al., 2004), and human health (e.g., Bhattachan et al., 2019; Comrie, 2005; Kanatani et al., 2010; O'Hara et al., 2000).

Dust emission generally occurs as a result of saltation at the land surface (Gillette, 1977). Saltation, in turn, occurs when the force of the wind on the surface exceeds, at least in some places, the forces holding sand-sized particles (i.e., the particles that saltate and that have the lowest threshold for movement) in place (Bagnold, 1941; Marticorena and Bergametti, 1995). Dust is emitted when saltating particles strike the surface and impart sufficient energy to emit suspension-sized particles (<~50 μm) that are carried downwind as “dust” (e.g., Gillette, 1977; Kok, 2010; Zender et al., 2003).

Several factors affect the susceptibility of the surface to aeolian transport. The threshold for initiating saltation on a dry soil, for example, depends on soil texture, organic matter, salt content, disturbance, and recent meteorology (Gillette, 1988; Gillette et al., 1980; Webb et al., 2016). The presence of soil moisture, either as a result of precipitation or adsorbed from the atmosphere, generally increases the threshold for transport (Fecan et al., 1999; Ravi et al., 2004). The amount of clay influences the efficiency of dust production once saltation occurs (Gillette, 1974; Marticorena and Bergametti, 1995).

Roughness, anything that impedes the horizontal flow of the wind, also modulates aeolian transport (Chepil, 1950). Vegetation is a key type of roughness. Roughness impacts aeolian transport by covering the soil surface, extracting momentum from the wind, and trapping airborne particles (Gillies et al., 2007; King et al., 2005; Marticorena and Bergametti, 1995; Okin, 2008; Raupach et al., 1993; Webb et al., 2014; Wolfe and Nickling, 1993). Although there are alternate models for how vegetation affects aeolian transport, nearly all agree that the vertical structure of vegetation is important in modulating the wind shear stress exerted on the surface (Marticorena and Bergametti, 1995; Okin, 2008;

E-mail address: okin@ucla.edu.

https://doi.org/10.1016/j.rse.2023.113581
Received 16 September 2022; Received in revised form 31 March 2023; Accepted 11 April 2023
Available online 19 April 2023

Raupach et al., 1993; Shao, 2001). One of the most important parameters used to characterize vertical structure is *lateral cover*, *L* (sometimes referred to as λ, but here λ is reserved for wavelength) which is defined as (Lancaster and Baas, 1998):

$$L = \frac{nwh}{S} = Nwh \tag{1}$$

where *n* is the number of roughness objects in an area, *S*, *w* is the width of those objects, and *h* is the height of those objects. *N* is the number density:

$$N = \frac{n}{S}. \tag{2}$$

There is a long tradition of seeking to extract and use information on vertical structure in optical remote sensing. Perhaps one of the earliest efforts is that of Richardson et al. (1975), which was followed by the those of Li and Strahler (1985, 1986) and Franklin and Strahler (1988) from which current operational BRDF models can trace their lineage (e.g., Schaaf et al., 2002). Since, there have been countless remote sensing papers that have made use of the shade/shadow that is inherent in optical remote sensing data over rough surfaces (e.g., Asner et al., 1997; Estes et al., 2010; Fitzgerald et al., 2005; Franklin and Turner, 1992; Li et al., 2005; Mustard, 1993; Roberts et al., 1997; Roberts et al., 1993; Scarth and Phinn, 2000).

Over the past decade, several papers (Chappell et al., 2010; Chappell and Webb, 2016; Chappell et al., 2018; Hennen et al., 2022; Marticorena et al., 2004) have argued for an approach to estimating vegetation roughness from remotely sensed data that focuses on shade. It is easy to see why such an approach might hold promise. A very simple model can be used to understand the fundamental relationship between shadow and lateral cover: a flat surface covered with a population of square cuboids, illuminated at a zenith angle, θ (Fig. 1). As long as the objects are sparse enough, or the illumination angle is high enough, the shadows from one object will not intersect another object or its shadow. In this case, the horizontal projection of the shadow for each object will have an area of $whtan\theta$ and the fractional area that is covered in shadow will simply be:

$$f_s = Nwhtan\theta = Ltan\theta. \tag{3}$$

From this simple relationship, it is clear that the degree of shade in any pixel should be related to the number and size of objects in the pixel, as well as the solar zenith angle. Other factors could affect the fraction of shade, such as the optical porosity of the objects which would cause them to cast less shadow, but under normal circumstances there should generally be a relationship between shade fraction, the number and geometry of objects, and the angle at which they are illuminated.

The model suggested by Chappell et al. (2010; 2016; 2018) argues that the "normalized (at-nadir) hemispherical albedo" should be related to surface roughness (specifically lateral cover, *L*, e.g., Fig. 5 in Chappell et al., 2018). Normalized (at-nadir) hemispherical albedo is defined (eq. 4 in Chappell et al., 2018) as

$$\omega_n = \frac{1-\rho(\lambda)}{\rho(\lambda,0)}, \tag{4}$$

where $\rho(\lambda)$ is the nadir-looking hemispherical-directional reflectance factor (HDRF) of a surface (that is, illuminated from the full hemisphere but observed only at zenith, which is to say, nadir-looking) at wavelength, λ, and $\rho(\lambda,0)$ is the nadir-looking bidirectional reflectance factor (BRF) at illumination angle $\theta = 0$, i.e. illuminated and observed from zenith. The definitive reflectance terminology of Schaepman-Strub et al. (2006) has been used to avoid confusion based on inconsistent and incorrect use of terms (especially "albedo") in the literature.

Here, the use of ω_n to estimate surface roughness, most specifically as a measure of *L*, is evaluated. First, geometric-optical modeling is presented to show that ω_n is not spectrally independent. Second, ω_n is calculated from real MODIS BRDF data to show that there is little empirical evidence for its spectral independence. Additionally, some practical considerations concerning use of MODIS albedo and the calculation of ω_n are discussed. Finally, some theoretically sound ideas for estimation of *L* from MODIS data are presented.

2. Methods

Most natural surfaces are not spectrally 'flat'; that is, they have different apparent reflectance at different wavelengths. Many remote sensing techniques aimed at determining the composition of the Earth's surface make use of this spectral information. This is even true of simple vegetation indices, such as the commonly-used normalized difference vegetation index (NDVI), which gains its power from differences in reflectance between the red and near-infrared portions of the spectrum (Tucker, 1979). For mathematical approaches that do not use spectral information, and instead use data from a single spectral band, it is important to note that wavelength-dependence and reflectance-dependence mean the same thing. That is, the result of a calculation made with a single reflectance value is dependent upon that value, whether it varies because of changing surface reflectance at a single wavelength or because a specific value of reflectance at a given wavelength is used. The approach suggested by Chappell and Webb (2016) and Chappell et al. (2018) is a single-wavelength approach. Thus, in the following, wavelength-dependence (e.g., dependence of reflectance on wavelength, $\rho(\lambda)$) refers to reflectance at a specific wavelength or spectral band rather than the shape of the relationship between reflectance and wavelength.

2.1. Geometric-optical modeling

Using the simple model shown in Fig. 1, the bidirectional reflectance factor (BRF, illuminated from a single direction, observed from a single direction) of the surface can be derived. Assuming linear mixing (i.e., assuming no multiple scattering and consistent with Chappell et al., 2010, 2018, e.g., Shimabukuro and Smith, 1991), the BRF of the surface, will be

$$\rho_p(\lambda,\theta) = f_c\rho_c(\lambda) + f_b(\theta)\rho_b(\lambda) + f_s(\theta)\rho_s(\lambda), \tag{5}$$

where $\rho_p(\lambda,\theta)$ is the modeled BRF of a nadir-looking instantaneous field of view (or, pixel, *p*) and $\rho_c(\lambda)$, $\rho_b(\lambda)$, and $\rho_s(\lambda)$ refer to the BRF of the top

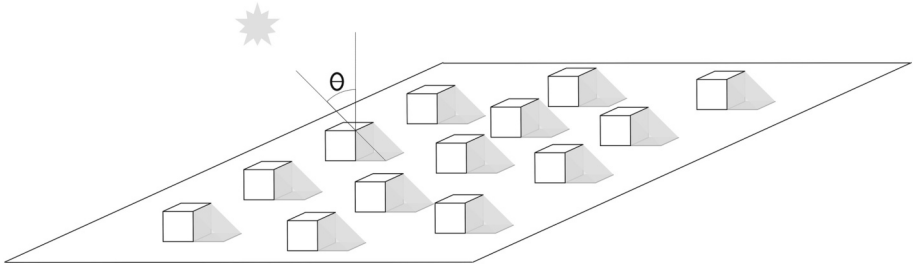

Fig. 1. Conceptual model of a field of cuboids, illuminated at angle θ, casting shadows on the background.

of the cuboid, background, and shade, respectively (see also Supplement 1). f_b and f_s are functions of θ because the amount of shaded and unshaded background depends on illumination angle. The area of the flat surface of the top of the cuboids is not θ-dependent. If it is assumed that shade is photogrammetric, $\rho_s(\lambda) = 0$ (Roberts et al., 1998), then

$$\rho_p(\lambda,\theta) = f_c\rho_c(\lambda) + f_b(\theta)\rho_b(\lambda). \quad (6)$$

In the special case where $\rho_c(\lambda) = \rho_b(\lambda) = \rho(\lambda)$, this reduces to:

$$\rho_p(\lambda,\theta) = \rho(\lambda)(f_c + f_b(\theta)), \quad (7)$$

and because $f_c + f_b(\theta) + f_s(\theta) = 1$, this becomes

$$\rho_p(\lambda,\theta) = \rho(\lambda)(1 - f_s(\theta)). \quad (8)$$

When illuminated from above, i.e., $\theta = 0$, $f_s(0) = 0$, and so

$$\rho_p(\lambda,0) = \rho(\lambda). \quad (9)$$

Replacing $\rho(\lambda)$ in eq. (4) with $\rho_p(\lambda,\theta)$ and $\rho(\lambda,0)$ with $\rho_p(\lambda,0)$, ω_n becomes

$$\omega_n = \frac{1-\rho(\lambda)(1-f_s(\theta))}{\rho(\lambda)} = \frac{1-\rho(\lambda)}{\rho(\lambda)} + f_s(\theta). \quad (10)$$

Substituting eq. 3 yields

$$\omega_n = \frac{1-\rho(\lambda)}{\rho(\lambda)} + Ltan\theta. \quad (11)$$

This model is limited to cases where the shadow of one cuboid cannot shade another, either due to too-close spacing or too-high illumination angle (θ), with the condition that the model is only valid where

$$N < \frac{1}{(htan\theta + w)^2}. \quad (12)$$

It may be argued that eq. 11 is not applicable, however, even for the narrow range of θ-N combinations where there is no self-shading, because the term in the numerator in eq. 4, $\rho(\lambda)$, should really be the integral of the nadir-looking BRF over a range of θ (0°-90°, Chappell and Webb, 2016), hence why it was originally called "hemispherical albedo" (the term "albedo" is ambiguous, but is generally only used to refer to hemispherical measurements of reflected radiation, rather than directional measurement of hemispherical illumination, which is termed "hemispherical-directional reflectance factor (HDRF)" and is what Chappell and Webb (2016) and Chappell et al. (2018) have reported, see Schaepman-Strub et al., 2006). To derive HDRF, eq. 8 can be integrated, taking $f_s = Ltan\theta$ (eq. 3) and including cosine-dependence of ρ_p on θ to get

$$\int_0^b \rho_p(\lambda,\theta)cos(\theta)d\theta = \int_0^b \rho(\lambda)cos(\theta)(1-f_s(\theta))d\theta = \rho(\lambda)(L(cos(b)-1) + sin(b)), \quad (13)$$

where b is the upper limit of integration and must be $0° < b < 90°$. In this case, eq. 4 becomes

$$\omega_n = \frac{1-\rho(\lambda)(L(cos(b)-1)+sin(b))}{\rho(\lambda)}, \quad (14)$$

which gives a linear relationship between L and ω_n (for a specific b) with positive slope depending on b.

2.2. MODIS data analysis of spectral dependence

Analytical models are not the only way to evaluate the use of MODIS MCD43A3 data to estimate roughness for dust modeling; MODIS data themselves can be used to investigate the practicalities of this approach. Whereas the geometric-optical considerations above focused mainly on evaluation of BRF and HDRF in the numerator of eq. 4, this section will focus on the denominator. Specifically, the proposed proxies for $\rho(\lambda,0)$. The purpose is to evaluate whether proxies for $\rho(\lambda,0)$ really can yield estimates of ω_n that are spectrally independent.

Note that, in eq. 4, the purpose of dividing $1-\rho(\lambda)$, which has directional dependence, by $\rho(\lambda,0)$, which does not have directional dependence is to ensure that $\omega_n$is not dependent upon reflectance or wavelength. Chappell and Webb (2016) suggests the MCD43A3 f_{iso} quantity as the normalization constant, whereas Chappell et al. (2018) also suggests MODIS MCD43A4 nadir BRDF-adjusted reflectance (NBAR) as a candidate.

In order for ω_{ns} (ω_n scaled to physically reasonable units) to be used any modeling context, it must be wavelength-independent. If it were not, the user would be forced to decided why ω_{ns} calculated using one band is "right" and that calculated using another band is "wrong" for a particular modeling application, and there is no reason to believe that results at different wavelengths would be simply proportional (thus allowing simple intra-band calibrations). ω_{ns} is defined as

$$\omega_{ns} = \frac{(a-b)(\omega_n - \omega_{n,max})}{\omega_{n,min} - \omega_{n,max}} + b, \quad (15)$$

where a and b are scaling constants and $\omega_{n,min}$ and $\omega_{n,max}$ represent the minimum and maximum values of range over which ω_n is scaled. Assuming that $\omega_{n,min} = 0$ (as it is in Ziegler et al., 2020), this equation can be rewritten as:

$$\omega_{ns} = c_\lambda\omega_{n,\lambda} + a, \quad (16)$$

where

$$c_\lambda = \frac{(b-a)}{\omega_{n,max}}. \quad (17)$$

c_λ and $\omega_{n,\lambda}$ are subscripted with λ to indicate that c_λ may be wavelength-dependent (at least because $\omega_{n,max}$ may be wavelength-dependent).

This relationship can be viewed in two ways that are conceptually different but equivalent in terms of import. First, if $a \ll c_\lambda\omega_{n,\lambda}$ in eq. 16, then the ratio of $\omega_{n,\lambda}$ calculated with any two bands gives

$$\frac{\omega_{n,1}}{\omega_{n,2}} \approx \frac{c_2}{c_1}. \quad (18)$$

Second, rearranging eq. 16 yields

$$\omega_{n,\lambda} = \frac{\omega_{ns} - a}{c_\lambda}. \quad (19)$$

To work with eq. 19, we can start by assuming that ω_{ns} is wavelength-independent because normalization by some reflectance-related value in eq. 4 makes it so. a must be wavelength-independent because it refers to lab-derived lateral cover, defined without reference to light in any way. Therefore, under this assumption, $\omega_{ns} - a$ must be a constant

$$\frac{\omega_{n,1}}{\omega_{n,2}} = \frac{c_2}{c_1}. \quad (20)$$

In other words, if ω_{ns} really is wavelength-independent, then the ratio of values of ω_n calculated with two different MODIS bands should be a constant (that is, should have the same value everywhere). If we find that the ratio of ω_n calculated with two different MODIS bands is *not* constant (or nearly so, to account for noise), then the assumption that ω_{ns} is wavelength-independent must also be wrong (*reductio ad absurdum*).

To investigate empirically, MODIS MCD43 data from a portion of the Texas Panhandle were downloaded from AppEEARS (https://appeears.earthdatacloud.nasa.gov/) including the "black sky albedo" (BSA), f_{iso}, f_{geo}, and NBAR for August 1, 2010. This location was chosen because this area has been investigated by Hennen et al. (2022) in an application of the Chappell and Webb (2016) approach to estimate dust emission. The . JSON file needed to reproduce this search has been included as

Supplement 2, as well as IDL (L3 Harris Geospatial Solutions, Inc.) code used to do calculations after stacking the images, which were done in ENVI to retain information about the data source for each band. The header for the input file for the IDL code is also included in Supplement 2 so that anyone might view the image stacking and see exactly which files were used.

3. Results and discussion

3.1. Geometric-optical modeling

Eq. 11 indicates that for the simplest model (Fig. 1), ω_n should have a positive, linear relationship with L, where the slope depends on the illumination angle. In addition, however, ω_n has a strong negative relationship with $\rho(\lambda)$ (Fig. 2). This result directly contradicts the claim by Chappell et al. (2018), p. 762): "These results suggest that the normalisation removed the spectral dependence".

When HDRF is included in the estimation of ω_n (eq. 14) once again, there is a strong negative relationship with $\rho(\lambda)$, which will essentially set the intercept on the ω_n vs. L line (Fig. 2).

Thus, the normalization of $(1-\rho(\lambda,\theta))$ by $\rho(\lambda,0)$ does not appear to remove dependence upon intrinsic reflectance. By extension, this normalization also does not remove dependence upon wavelength, since reflectance is a function of wavelength. It may be countered that the model presented up to now is unlike that of Chappell et al. (2010) and subsequent papers because the reflectance, $\rho(\lambda)$, for both the background and objects were assumed to be the same. Or, it might be argued that the cuboids are unlike the hemispheroids used in Chappell et al. (2010). Or, it might be argued that the model presented here doesn't allow self-shading. Or, it might be argued that the model above does not include a cosine dependence upon illumination angle; although, it might be said that the Chappell et al. (2010; 2016; 2018) models also do not include the cosine effect. In response, three additional models (cuboids, prisms, hemispheroids) have been derived which, together, address each of these concerns by including, variously, cosine-dependence, hemispheroids, and self-shading (Supplement 1).

The results of this modeling (Fig. 3) shows dependence of ω_n on object shape, background reflectance, object reflectance, and illumination angle. Chappell and Webb (2016) propose a linear correction for ω_n (their eq. 6) that can be used to estimate L (fig. 6 in Chappell et al., 2018) from MODIS data. The modeling results presented here highlight the weakness of this approach; the intercept and slope of any relationship between ω_n and L depends upon the unknown intrinsic reflectance of the roughness elements and background in a field of view. In fact, in some cases, as when background reflectance is low and roughness element reflectance is high, the relationship between ω_n and L has a negative slope (Fig. 3). Therefore, there can be no universal set of calibration coefficients (a and b in eq. 7 of Chappell et al., 2018) and the intercept of this relationship is exceptionally sensitive to the surface reflectance which is not known a priori (for the simplest case, see eq. 11).

Furthermore, from a geometric-optical perspective, the attempt to implement the use of ω_n to estimate surface roughness from MODIS "black sky albedo" data is logically inconsistent with the ray casting done by Chappell et al. (2010; 2016; 2018). In an attempt to maintain a precise vocabulary, the quantity that is reported as "black sky albedo" in the MODIS product suite (Lucht et al., 2000) is here referred to as directional–hemispherical reflectance (DHR) where reflected light, with a directional source, is integrated across the outgoing hemisphere (this term is sometimes described as "albedo" in the scientific literature, e.g., Martonchik (1994), but the term "albedo" is imprecise, in part, due to its various uses across the sciences). Chappell et al. (2018) use MODIS DHR (e.g., MCD43A3 MODIS black sky albedo) in the numerator of the equation used to estimate ω_n (eq. 4), assuming "that the MODIS $\omega_{dir}(0°,\lambda)$ [$\rho(\lambda)$, in the symbology used here] was reciprocal to our ray-casting model which used at-nadir view angle and integrates illumination angle" (p. 760). That is to say, the authors wish to equate HDRF and

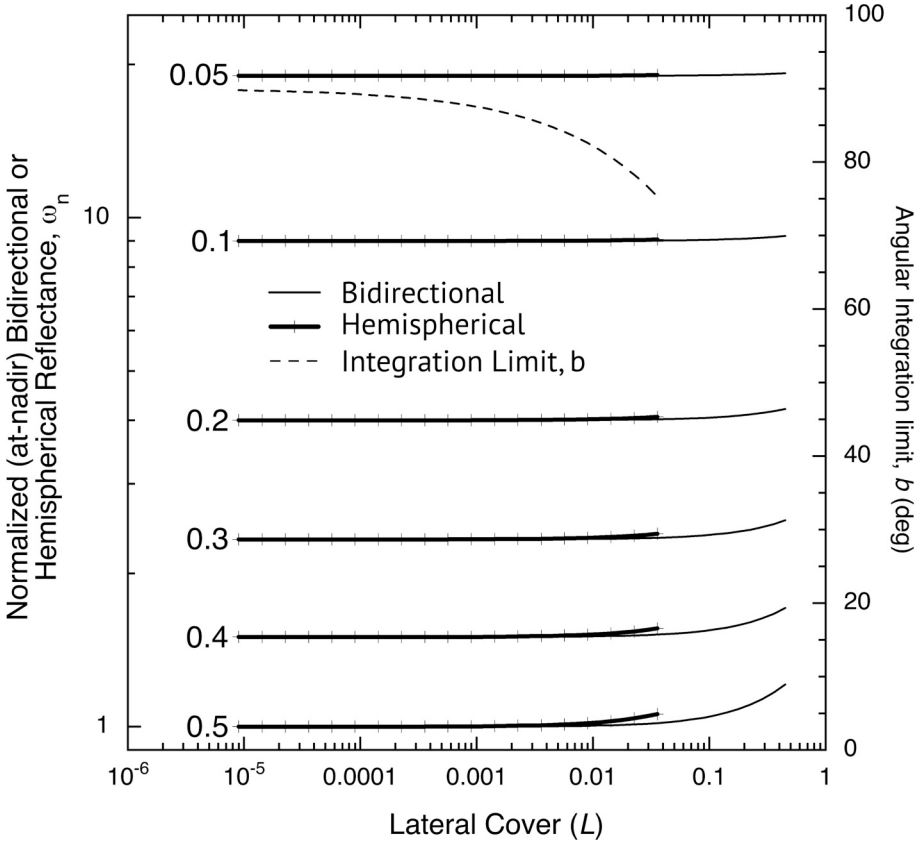

Fig. 2. Plot showing ω_n as a function of lateral cover for different values of $\rho(\lambda)$ (numbers) using eq. 11 for the normalized bidirectional reflectance and eq. 14 for the normalized hemispherical-directional reflectance. In both cases, the intercept varies by over an order of magnitude for the range of $\rho(\lambda)$ considered. For a given L, the angular integration limit (eqs. 13 and 14), b, was calculated as the maximum angle at which the model assumptions hold (using eqs. 3 and 12). Hemispherical ω_n was not calculated for values of L where the maximum angle $<75°$.

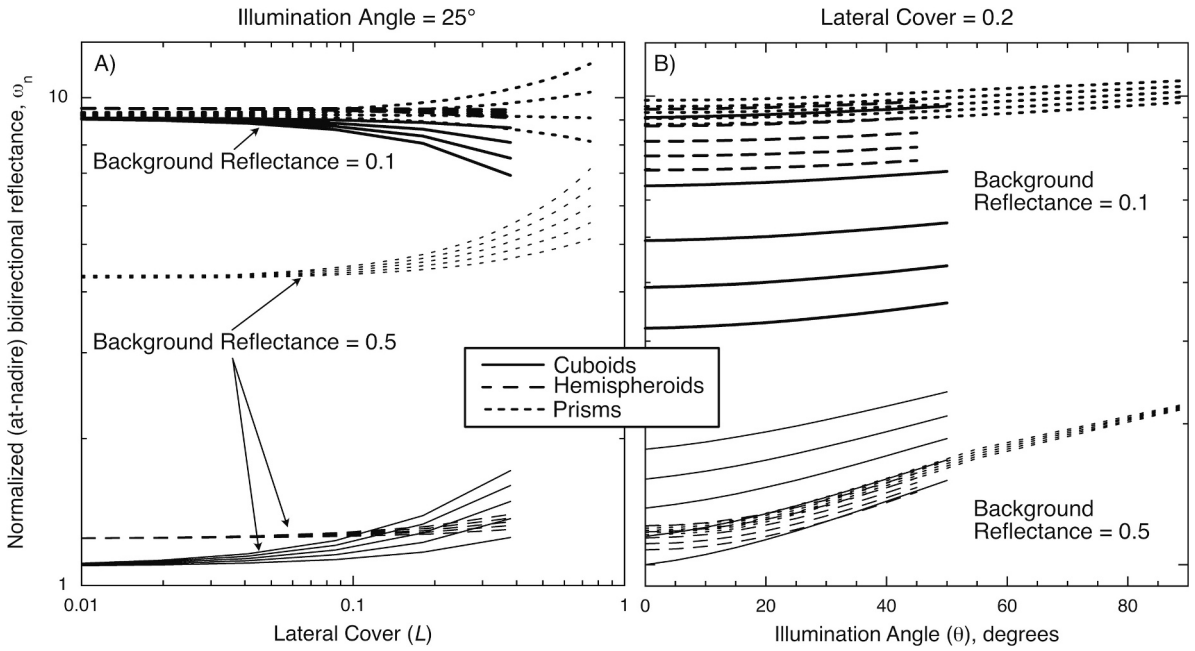

Fig. 3. Modeled ω_n for different-shaped objects with reflectance different from the background (See Supplement 1 for details). A) Illumination angle, θ, is constant for all values of lateral cover, *L*. B) Lateral cover, *L*, is constant for all values of illumination angle, θ. For any shape/background reflectance family of curves, the curve with the lowest ω_n has the highest object reflectance. Curves are only plotted where the model assumptions have not been violated. The prism model is valid at higher levels of both *L* and θ because this model explicitly allows self-shading.

DHR. However, the hemispherical directional reflectance factor (HDRF) calculated from ray-tracing in Chappell et al. (2010; 2016; 2018) cannot be substituted for DHR estimated by the MODIS MCD43A3 product, especially in the present context because DHR is sensitive to θ, but the HDRF used by Chappell et al. (2010; 2016; 2018) is not. Because the shade cast by roughness on the surface is directly related to θ (e.g., eq. 3), MODIS DHR must be sensitive to solar zenith angle. A close reading of Schaaf et al. (2002) and other materials related to the MODIS albedo product shows that "the MCD43A3 Albedo Product (MODIS/Terra Albedo Daily L3 Global 500m SIN Grid) provides both the white-sky albedos and the black-sky albedos (at local solar noon)" (Schaaf, 2022). For a mid-latitude desert (30°), the solar zenith angle at solar noon is 53.4° on the winter solstice and 6.6° on the summer solstice. The amount of shadow cast by roughness in the winter in a mid-latitude desert that might produce dust is an order of magnitude greater than that cast in summer (tan(53.4)/tan(6.6) = 11.7, eq. 3) even if the amount of roughness remains the same. Modeling that used wintertime MCD43A3 data would, therefore, estimate significantly less dust than the same model using summertime MCD43A3 data.

3.2. MODIS data analysis of spectral dependence

Values of NBAR calculated for each band for the test area are clearly different (sometimes dramatically, Table 1), likewise for ω_n (Table 2), giving no indication that ω_n is wavelength (and reflectance) independent. Indeed, the CV for the NBAR for each band is roughly the same as

Table 1
NBAR minimum, maximum, mean, and CV values by band.

	minimum	maximum	mean	CV
MODIS Band 1 (620–670 nm)	0.06	0.25	0.12	0.25
MODIS Band 2 (841–876 nm)	0.21	0.45	0.32	0.13
MODIS Band 3 (459–479 nm)	0.02	0.12	0.04	0.22
MODIS Band 4 (545–565 nm)	0.06	0.18	0.09	0.15
MODIS Band 5 (1230–1250 nm)	0.27	0.44	0.34	0.08
MODIS Band 6 (1626–1652 nm)	0.21	0.48	0.3	0.12
MODIS Band 7 (2105–2155 nm)	0.11	0.4	0.21	0.22

Table 2
ω_n minimum, maximum, mean, and CV values by band.

	minimum	maximum	mean	CV
MODIS Band 1 (620–670 nm)	1.98	16.26	5.7	0.31
MODIS Band 2 (841–876 nm)	0.89	3.64	1.89	0.26
MODIS Band 3 (459–479 nm)	4.67	46.62	17.72	0.26
MODIS Band 4 (545–565 nm)	2.83	14.42	8.09	0.18
MODIS Band 5 (1230–1250 nm)	1.05	2.57	1.58	0.16
MODIS Band 6 (1626–1652 nm)	0.95	3.79	1.82	0.18
MODIS Band 7 (2105–2155 nm)	1.08	7.48	2.84	0.27

the CV for ω_n, indicating that much of the variability measured in ω_n can be explained merely by the value of the reflectance. When ω_n plotted versus BSA (Fig. 4, black), a hyperboloid curve is apparent, consistent with simply plotting (1-BSA)/BSA (Fig. 4, grey). The deviation of the

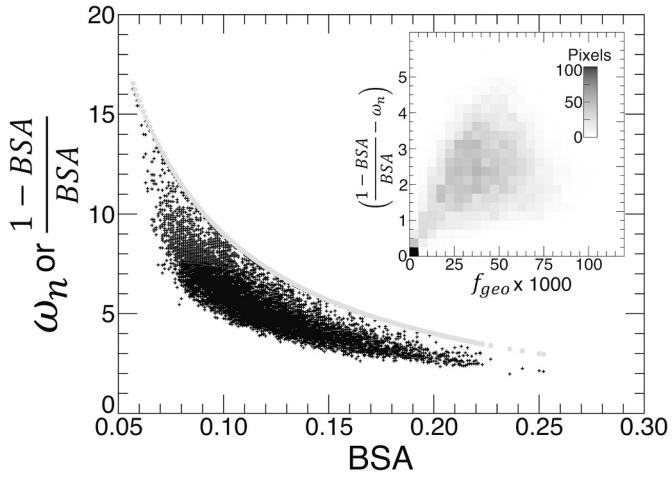

Fig. 4. Scatterplot of ω_n (black symbols) and (1-BSA)/BSA (grey symbols) vs BSA for MODIS MCD43B4 band 1. Inset: Density plot of $\left(\frac{1-BSA}{BSA} - \omega_n\right)$ vs. MODIS MCD43B4 f_{geo}(x 1000).

black points from the grey points appears to be positively related to the geometric scattering components in the MODIS BRDF model (Fig. 4, inset). In other words, there is little indication that the information contained in ω_n differs in novel ways from (1-BSA)/BSA, and what differences do exist appear to largely replicate the information present in the geometric component of the MODIS BRDF inversion model (i.e., f_{geo}). There is absolutely information about vegetation structure in f_{geo}, which derive ultimately from a geometric-optical model of discrete vegetation canopies (Li and Strahler, 1992; Schaaf et al., 2002), but it is not yet clear how those model parameters or the geometric-optical kernel might be related to parameters that influence dust emission.

Calculation of $c_\lambda\langle\omega_{n,\lambda}\rangle/a$, assuming $a = 0.0001$ (Ziegler et al., 2020) indicates that a is one-to-two orders of magnitude less than $c_\lambda\langle\omega_{n,\lambda}\rangle$ (Table 3), therefore we can confirm that $a \ll c_\lambda\omega_{n,\lambda}$, and thus $\frac{\omega_{n,x}}{\omega_{n,1}}$ should be roughly constant (i.e., $\approx \frac{c_2}{c_1}$, eq. 18). However, the ratio of ω_n calculated for MODIS bands 2–7 to that calculated from MODIS band 1, shows no indication that that this ratio is a constant Table 3. Indeed, the CV is also nearly the same as for the NBAR (Table 1). Therefore, using either of the lines of argument made above ($a \ll c_\nu\omega_{n,\nu}$ or *reductio ad absurdum*), there appears to be little empirical support for ω_{ns} being independent of either wavelength or underlying reflectance.

Finally, some additional considerations on the use of MODIS BSA, NBAR, and f_{iso} parameters in eq. 4 are important when evaluating whether the approach of Chappell et al. (2010; 2016; 2018) should be used to improve estimates of dust emission. First, MODIS BSA is not, strictly speaking, a quantity that can be validated against field measurements. In practical terms, BSA is a theoretical construct where illumination is from a single direction, without any diffuse component. There are no daytime measurements that could be made in natural environments on Earth where there is no diffuse light contribution to the incident radiation. Therefore, the uncertainty of BSA is unquantified and unquantifiable. Likewise, as a kernel fitting parameter in a model, f_{iso} cannot be validated. In consequence, even if the MODIS NBAR, which uses f_{iso}, has a high accuracy, there is no way to determine the uncertainty of f_{iso} itself. Any relationship of the form $(1 - X)/X$, such as eq. 4, is highly sensitive to the uncertainty of X (Fig. 5). For example, if f_{iso} had an uncertainty of 10%, and assuming $f_{iso} \approx$ BSA$= X =$0.4, uncertainty in $\omega_n$of over 125% should be expected. If the uncertainty of f_{iso} is 1%, this still results in a 12.5% uncertainty in ω_n. Thus, the form of eq. 4 is a particularly unfortunate formulation that has low resilience to uncertainty/error. Last, 16-day MODIS composites are comprised of data from a range of viewing angles (Schaaf et al., 2002), with the instantaneous fields of view (IFOVs) at the outside of the swath being observed from 58.8° (the outermost IFOV is 1165 km from the nadir point in MODIS's 2330-km swath and MODIS is at an altitude of ~705 km, therefore arctan(1165/705) = 58.8°, Barnes et al., 1998). The nominal ground instantaneous field of view (GIFOV) at nadir for MODIS is 500 m, but projected to the outside of the swath, the same IFOV will result in an along-track GIFOV of 500 m/cos(58.8°) = 965 m. Thus, MODIS BRDF products, even for one point on the surface, are inherently derived from a range of actual GIFOVs. This mixing pixel issue could potentially lead to greater problems than any lateral cover model itself, especially given the form of eq. 4.

Table 3
$c_\lambda\langle\omega_{n,\lambda}\rangle/a$ by band assuming $a = 0.0001$ as in Ziegler et al. (2020) and minimum, maximum, mean, and median values of $\frac{\omega_{n,x}}{\omega_{n,1}}$ by band.

	$c_\lambda\langle\omega_{n,\lambda}\rangle/a$	Minimum $\frac{\omega_{n,x}}{\omega_{n,1}}$	Maximum $\frac{\omega_{n,x}}{\omega_{n,1}}$	Mean $\frac{\omega_{n,x}}{\omega_{n,1}}$	CV $\frac{\omega_{n,x}}{\omega_{n,1}}$
MODIS Band 2 (841–876 nm)	162.78	0.06	0.71	0.35	0.31
MODIS Band 3 (459–479 nm)	53.83	1.94	5.14	3.18	0.14
MODIS Band 4 (545–565 nm)	505.76	0.77	2.43	1.48	0.16
MODIS Band 5 (1230–1250 nm)	230.98	0.09	0.63	0.29	0.24
MODIS Band 6 (1626–1652 nm)	45.09	0.17	0.6	0.33	0.15
MODIS Band 7 (2105–2155 nm)	52.05	0.33	0.81	0.5	0.11

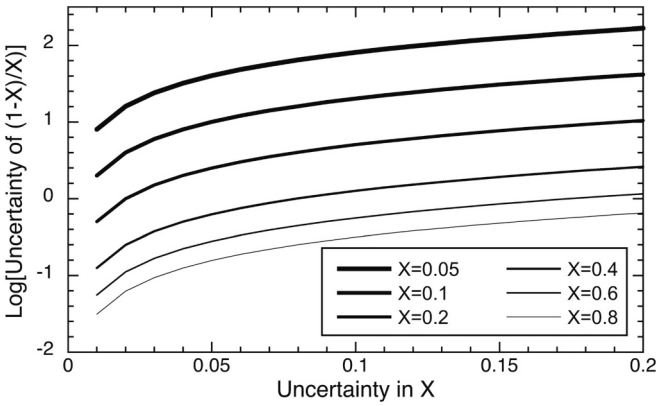

Fig. 5. Uncertainty of (1-X)/X vs. Uncertainty of X for different values of X.

4. Conclusions

Based on geometric-optical modeling and analysis of MODIS data, there appears to be little support for the use of the MODIS-based estimation of surface parameters related to dust emission as proposed by Chappell et al. (2010; 2016; 2018). The results of subsequent papers that use this method (e.g., Hennen et al., 2022; Ziegler et al., 2020) should be reconsidered, and this approach should not be introduced into prognostic models of dust emission.

However, modeling does suggest that there should be a relationship between shade fraction, roughness density (specifically, lateral cover), and solar zenith angle. And therefore, there may yet be optical remote sensing-based methods that can provide direct information about surface roughness that might improve on methods in existing dust emission models (models which currently use NDVI, vegetation cover, leaf area index to infer the effect of vegetation on dust emission, e.g., Darmenova et al., 2009; Zender et al., 2003).

There are likely many optical remote sensing approaches that might be investigated for their usefulness in determining the vertical structure of surface roughness. Two such approaches that employ logic like that in the simple geometric-optical modeling presented here, the heritage of which goes back at least to Li and Strahler (1985, 1986) and Franklin and Strahler (1988), are:

1) Estimate shade directly and combine this with information on solar zenith angle to infer roughness length (e.g., eq. 3). There have been many studies that have estimated shade fraction from optical remote sensing data over rough surfaces (e.g., Asner et al., 1997; Estes et al., 2010; Fitzgerald et al., 2005; Franklin and Turner, 1992; Li et al., 2005; Mustard, 1993; Roberts et al., 1997; Roberts et al., 1993; Scarth and Phinn, 2000). By using all of the spectral information in remote sensing data, variations in vegetation cover and greenness can be accounted for (e.g., Okin, 2010), and such efforts would rest on a long history of spectral unmixing in the remote sensing literature. Although the uncertainty in vegetation and shade estimation is greater for multispectral data (e.g., Landsat and MODIS) compared to imaging spectrometer data (e.g., Guerschman et al., 2009), there may still be incremental improvements brought to bear. The value of this approach will likely increase with the increasing availability of spaceborne imaging spectrometer data.

2) Use seasonal changes in solar zenith to estimate lateral cover. Eq. 3 suggests that f_s should depend upon solar zenith angle. For surface where the roughness does not change between seasons (i.e., mainly surfaces where the roughness is due to pebbles, rocks, and other geological roughness), temporal differences in f_s should relate directly to lateral cover. Any approach that estimates seasonal changes in brightness, where those differences are due only to shading (including, but not limited to spectral unmixing), should provide some information about roughness that might be included in novel dust emission schemes.

Finally, there may be opportunities to utilize information from the geometric kernel of the MODIS BRDF model itself (e.g., Fig. 4, inset). Tracing its heritage as it does to geometric-optical models that explicitly consider the amount and size of roughness elements (Li and Strahler, 1992; Schaaf et al., 2002), it is reasonable to expect that roughness information is embedded in the current MODIS BRDF model. Indeed, the MODIS BRDF model is similar to that used for the POLarization and Directionality of Earth's Reflectance (POLDER) mission (Roujean et al., 1992; Roujean et al., 1997), from which a kernel-derived "protrusion coefficient" was related to surface roughness (Marticorena et al., 2004). Similarly, there may be a way to exploit and validate kernel-based roughness information in MODIS, though that would require considerable new research.

Author credit statement

Okin is the sole author of this paper and is solely responsible for all aspects of its creation.

Declaration of Competing Interest

The authors declare the following financial interests/personal relationships which may be considered as potential competing interests: Gregory S Okin reports financial support was provided by NASA. Gregory S Okin reports financial support was provided by National Science Foundation.

Data availability

Data available from public repositories

Acknowledgments

This work was partially supported by funding from the National Science Foundation to 1) New Mexico State University for the Jornada Basin Long-Term Ecological Research Program (DEB 2025166) and 2) University of California Los Angeles (DEB 1556735). The work was also supported by the NASA EMIT mission (UCLA subcontract from main JPL contract NASA: 80NM0018D0004).

Appendix A. Supplementary data

Supplementary data to this article can be found online at https://doi.org/10.1016/j.rse.2023.113581.

References

Asner, G., Wessman, C., Privette, J., 1997. Unmixing the directional reflectances of AVHRR sub-pixel landcovers. IEEE Trans. Geosci. Remote Sens. 35, 868–878.
Bagnold, R.A., 1941. The Physics of Blown Sand and Desert Dunes. Methuen, New York.
Barnes, W.L., Pagano, T.S., Salomonson, V.V., 1998. Prelaunch characteristics of the moderate resolution imaging spectroradiometer (MODIS) on EOS-AM1. IEEE Trans. Geosci. Remote Sens. 36, 1088–1100.
Bhattachan, A., Okin, G.S., Zhang, J., Vimal, S., Lettenmaier, D.P., 2019. Characterizing the role of wind and dust in traffic accidents in California. GeoHealth 3, 328–336.
Chappell, A., Van Pelt, S., Zobeck, T., Dong, Z., 2010. Estimating aerodynamic resistance of rough surfaces using angular reflectance. Remote Sens. Environ. 114, 1462–1470.
Chappell, A., Webb, N.P., 2016. Using albedo to reform wind erosion modelling, mapping and monitoring. Aeolian Res. 23, 63–78.
Chappell, A., Webb, N.P., Guerschman, J.P., Thomas, D.T., Mata, G., Handcock, R.N., Leys, J.F., Butler, H.J., 2018. Improving ground cover monitoring for wind erosion assessment using MODIS BRDF parameters. Remote Sens. Environ. 204, 756–768.
Chepil, W.S., 1950. Properties of soil which influence wind erosion: 1. The governing principle of surface roughness. Soil Sci. 69, 149–162.
Comrie, A.C., 2005. Climate factors influencing coccidioidomycosis seasonality and outbreaks. Environ. Health Perspect. 113, 688–692.
Darmenova, K., Sokolik, I.N., Shao, Y.P., Marticorena, B., Bergametti, G., 2009. Development of a physically based dust emission module within the weather research and forecasting (WRF) model: assessment of dust emission parameterizations and input parameters for source regions in central and East Asia. J. Geophys. Res.-Atmos. 114, D14201.
Estes, L.D., Reillo, P.R., Mwangi, A.G., Okin, G.S., Shugart, H.H., 2010. Remote sensing of structural complexity indices for habitat and species distribution modeling. Remote Sens. Environ. 114, 792–804.
Fecan, F., Marticorena, B., Bergametti, G., 1999. Parameterization of the increase of the aeolian erosion threshold wind friction velocity due to soil moisture for arid and semi-arid areas. Ann. Geophys.Atmos.Hydrospheres Space Sci. 17, 149–157.
Fitzgerald, G.J., Pinter Jr., P.J., Hunsaker, D.J., Clarke, T.R., 2005. Multiple shadow fractions in spectral mixture analysis of a cotton canopy. Remote Sens. Environ. 97, 526–539.
Franklin, J., Strahler, A.H., 1988. Invertible canopy reflectance modeling of vegetation structure in semiarid woodland. IEEE Trans. Geosci. Remote Sens. 26, 809–825.
Franklin, J., Turner, D.L., 1992. The application of a geometric optical canopy reflectance model to semiarid shrub vegetation. IEEE Trans. Geosci. Remote Sens. 30, 293–301.
Gillette, D.A., 1974. On the production of soil wind erosion aerosols having the potential for long range transport. J.Rech.Atmos. 8, 735–744.
Gillette, D.A., 1977. Fine particulate emissions due to wind erosion. Trans. Am. Soc. Agric. Eng. 20, 890–897.
Gillette, D.A., 1988. Threshold friction velocities for dust production for agricultural soils. J. Geophys. Res. 93, 12645–12662.
Gillette, D.A., Adams, J., Endo, A., Smith, D., Kihl, R., 1980. Threshold velocities for input of soil particles into the air by desert soils. J.Geograph.Res. 85, 5621–5630.
Gillies, J.A., Nickling, W.G., King, J., 2007. Shear stress partitioning in large patches of roughness in the atmospheric inertial sublayer. Bound.-Layer Meteorol. 122, 367–396.
Guerschman, J.P., Hill, M.J., Renzullo, L.J., Barrett, D.J., Marks, A.S., Botha, E.J., 2009. Estimating fractional cover of photosynthetic vegetation, non-photosynthetic vegetation and bare soil in the australian tropical savanna region upscaling the EO-1 hyperion and MODIS sensors. Remote Sens. Environ. 113, 928–945.
Hennen, M., Chappell, A., Edwards, B.L., Faist, A.M., Kandakji, T., Baddock, M.C., Wheeler, B., Tyree, G., Treminio, R., Webb, N.P., 2022. A North American dust emission climatology (2001–2020) calibrated to dust point sources from satellite observations. Aeolian Res. 54, 100766.
Jickells, T.D., An, Z.S., Andersen, K.K., Baker, A.R., Bergametti, G., Brooks, N., Cao, J.J., Boyd, P.W., Duce, R.A., Hunter, K.A., Kawahata, H., Kubilay, N., laRoche, J., Liss, P. S., Mahowald, N., Prospero, J.M., Ridgwell, A.J., Tegen, I., Torres, R., 2005. Global iron connections between desert dust, ocean biogeochemistry, and climate. Science 308, 67–71.
Kanatani, K.T., Ito, I., Al-Delaimy, W.K., Adachi, Y., Mathews, W.C., Ramsdell, J.W., 2010. Desert dust exposure is associated with increased risk of asthma hospitalization in children. Am. J. Respir. Crit. Care Med. 182, 1475–1481.
King, J., Nickling, W.G., Gillies, J.A., 2005. Representation of vegetation and other nonerodible elements in aeolian shear stress partitioning models for predicting transport threshold. J. Geophys.Res.Earth Surf. 110.
Kok, J.F., 2010. A scaling theory for the size distribution of emitted dust aerosols suggests climate models underestimate the size of the global dust cycle. Proc. Nat. Acad. Sci. USA 108, 1016–1021.
Lancaster, N., Baas, A., 1998. Influence of vegetation cover on sand transportation by wind: field studies at Owens Lake, California. Earth Surf. Process. Landf. 23, 69–82.
Li, L., Ustin, S.L., Lay, M., 2005. Application of multiple endmember spectral mixture analysis (MESMA) to AVIRIS imagery for coastal salt marsh mapping: a case study in China camp, CA, USA. Int. J. Remote Sens. 26, 5193–5207.
Li, X., Strahler, A.H., 1985. Geometric-optical modeling of a conifer forest. IEEE Trans. Geosci. Remote Sens. GE-23, 705–721.
Li, X., Strahler, A.H., 1992. Geometric-optical bidirectional reflectance modeling of the discrete crown vegetataion canopy: effect of crown shape and mutual shadowing. IEEE Trans. Geosci. Remote Sens. 30, 276–291.
Li, X.W., Strahler, A.H., 1986. Geometric-optical bidirectional reflectance modeling of a conifer forest canopy. IEEE Trans. Geosci. Remote Sens. 24, 906–919.
Lohmann, U., Feichter, J., 2005. Global indirect aerosol effects: a review. Atmos. Chem. Phys. 5, 715–737.
Lucht, W., Schaaf, C.B., Strahler, A.H., 2000. An algorithm for the retrieval of albedo from space using semiempirical BRDF models. IEEE Trans. Geosci. Remote Sens. 38, 977–998.
Mahowald, N.M., Baker, A.R., Bergametti, G., Brooks, N., Duce, R.A., Jickells, T.D., Kubilay, N., Prospero, J.M., Tegen, I., 2005. Atmospheric global dust cycle and iron inputs to the ocean. Glob. Biogeochem. Cycles 19.
Marticorena, B., Bergametti, G., 1995. Modeling the atmospheric dust cycle: 1. Design of a soil-derived dust emission scheme. J. Geophys. Res. 100, 16415–16430.
Marticorena, B., Chazette, P., Bergametti, G., Dulac, F., Legrand, M., 2004. Mapping the aerodynamic roughness length of desert surfaces from the POLDER/ADEOS bi-directional reflectance product. Int. J. Remote Sens. 25, 603–626.

Martonchik, J.V., 1994. Retrieval of surface directional reflectance properties using ground level multiangle measurements. Remote Sens. Environ. 50, 303–316.
Mustard, J.F., 1993. Relationships of soil, grass, and bedrock over the Kaweah serpentine melange through spectral mixture analysis of AVIRIS data. Remote Sens. Environ. 44, 293–308.
O'Hara, S.L., Wiggs, G.F.S., Mamedov, B., Davidson, G., Hubbard, R.B., 2000. Exposure to airborne dust contaminated with pesticide in the Aral Sea region. Lancet 355, 627–628.
Okin, G.S., 2008. A new model for wind erosion in the presence of vegetation. J.Geophys. Res.Earth Surf. 113, F02S10.
Okin, G.S., 2010. The contribution of brown vegetation to vegetation dynamics. Ecology 91, 743–755.
Okin, G.S., Mahowald, N., Chadwick, O.A., Artaxo, P., 2004. The impact of desert dust on the biogeochemistry of phosphorus in terrestrial ecosystems. Glob. Biogeochem. Cycles 18. https://doi.org/10.1029/2003GB002145.
Raupach, M.R., Gillette, D.A., Leys, J.F., 1993. The effect of roughness elements on wind erosion threshold. J. Geophys. Res. 98, 3023–3029.
Ravi, S., D'Odorico, P., Over, T.M., Zobeck, T.M., 2004. On the effect of air humidity on soil susceptibility to wind erosion: the case of air-dry soils. Geophys. Res. Lett. 31, L09501.
Richardson, A.J., Wiegand, C.L., Gausman, H.W., Cuellar, J.A., Gerbermann, A.H., 1975. Plant, soil, and shadow reflectance components of row crops. Photogramm. Eng. Remote Sens. 41, 1401–1407.
Roberts, D.A., Gardner, M., Church, R., Ustin, S., Scheer, G., Green, R.O., 1998. Mapping chaparral in the Santa Monica Mountains using multiple endmember spectral mixture models. Remote Sens. Environ. 65, 267–279.
Roberts, D.A., Green, R.O., Adams, J.B., 1997. Temporal and spatial patterns in vegetation and atmospheric properties from AVIRIS. Remote Sens. Environ. 62, 223–240.
Roberts, D.A., Smith, M.O., Adams, J.B., 1993. Green vegetation, nonphotosynthetic vegetation, and soils in AVIRIS data. Remote Sens. Environ. 44, 255–269.
Roujean, J.-L., Leroy, M., Deschamps, P.-Y., 1992. A bidirectional reflectance model of the Earth's surface for the correction of remote sensing data. J.Geophys.Res.Atmos. 97, 20455–20468.
Roujean, J.-L., Tanré, D., Bréon, F.-M., Deuzé, J.-L., 1997. Retrieval of land surface parameters from airborne POLDER bidirectional reflectance distribution function during HAPEX-Sahel. J.Geophys.Res.Atmos. 102, 11201–11218.
Scarth, P., Phinn, S., 2000. Determining forest structural attributes using an inverted geometric-optical model in mixed eucalypt forests, Southeast Queensland, Australia. Remote Sens. Environ. 71, 141–157.
Schaaf, C., 2022. MCD43A3 Albedo Product webpage accessed 9/11/22. In. https://www.umb.edu/spectralmass/terra_aqua_modis/v006/mcd43a3_albedo_product.
Schaaf, C.B., Gao, F., Strahler, A.H., Lucht, W., Li, X.W., Tsang, T., Strugnell, N.C., Zhang, X.Y., Jin, Y.F., Muller, J.P., Lewis, P., Barnsley, M., Hobson, P., Disney, M., Roberts, G., Dunderdale, M., Doll, C., d'Entremont, R.P., Hu, B.X., Liang, S.L., Privette, J.L., Roy, D., 2002. First operational BRDF, albedo nadir reflectance products from MODIS. Remote Sens. Environ. 83, 135–148.
Schaepman-Strub, G., Schaepman, M.E., Painter, T.H., Dangel, S., Martonchik, J.V., 2006. Reflectance quantities in optical remote sensing-definitions and case studies. Remote Sens. Environ. 103, 27–42.
Shao, Y., 2001. A model for mineral dust emission. J.Geophys.Res.Atmos. 106, 20239–20254.
Shimabukuro, Y.E., Smith, J.A., 1991. The least-squares mixing models to generate fraction images derived from remote sensing multispectral data. IEEE Trans. Geosci. Remote Sens. N1, 16–20.
Sokolik, I.N., Toon, O.B., 1996. Direct radiative forcing by anthropogenic airborne mineral aerosols. Nature 381, 681–683.
Tucker, C.J., 1979. Red and photographic infrared linear combinations for monitoring vegetation. Remote Sens. Environ. 8, 127–150.
Webb, N.P., Galloza, M.S., Zobeck, T.M., Herrick, J.E., 2016. Threshold wind velocity dynamics as a driver of aeolian sediment mass flux. Aeolian Res. 20, 45–58.
Webb, N.P., Okin, G.S., Brown, S., 2014. The effect of roughness elements on wind erosion: the importance of surface shear stress distribution. J. Geophys. Res.-Atmos. 119, 6066–6084.
Wolfe, S.A., Nickling, W.G., 1993. The protective role of sparse vegetation in wind erosion. Progr.Phys.Geogr.Earth Environ. 17, 50–68.
Yu, K., D'Odorico, P., Bhattachan, A., Okin, G.S., Evan, A.T., 2015. Dust-rainfall feedback in West African Sahel. Geophys. Res. Lett. 42, 7563–7571.
Zender, C.S., Bian, H., Newman, D., 2003. The mineral dust entrainment and deposition (DEAD) model: description and 1990s dust climatology. J. Geophys. Res. 108, 4416.
Ziegler, N.P., Webb, N.P., Chappell, A., LeGrand, S.L., 2020. Scale invariance of albedo-based wind friction velocity. J.Geophys.Res.Atmos. 125 e2019JD031978.